Shiomi *Earth, Planets and Space* (2017) 69:48
DOI 10.1186/s40623-017-0631-5

Earth, Planets and Space

LETTER Open Access

Dissimilar receiver functions observed at very close stations in the Kii Peninsula, central Japan: features and causes

Katsuhiko Shiomi*

Abstract

Receiver function analysis is one of the most powerful methods for modeling the subsurface structure beneath a seismograph station. Based on the assumption that similar receiver functions should be observed at stations located close to each other, we can construct a spatial distribution of a seismic velocity interface, such as the Moho discontinuity, to trace the distribution of *P*-to-*S* (*Ps*) converted phases in receiver functions. After more than 15 years of observation by the seismograph networks, we confirmed that receiver functions observed at two stations very close to each other in the Kii Peninsula, central Japan, show significantly different characteristics from each other. The backazimuth dependence of later phase arrivals within 4 s after the direct *P* wave was strong, especially for transverse components. Because the *Ps* converted phases at the Moho discontinuity arrived around 4 s after the direct *P* wave, we assume that the dissimilarity is caused by a localized structural anomaly in the crust. This assumption is supported by the fact that only the cross-correlation coefficients for the short-period transverse component of teleseismic waveforms were small. According to the geological map, the two stations are located in the accretionary complex along the Pacific coast, and the strikes of the geological boundaries show an abrupt change around the stations. Based on forward modeling with the anisotropic subsurface models, we confirmed that the characteristics of the observed receiver functions can be explained roughly by considering a localized anomaly in the upper and middle crust.

Keywords: Receiver function, Anisotropic crust, Accretionary complex, Kii Peninsula

Introduction

Receiver function (RF) analysis is one of the most powerful methods for modeling the underground structure beneath a seismograph station. The RF is calculated by deconvolution of the source wavelet from radial and transverse teleseismic waveforms, and it emphasizes the *P*-to-*S* (*Ps*) converted phases within *P* coda (e.g., Ammon 1991). The delay time of a converted phase from a direct *P* wave corresponds to the depth of the velocity interface where the converted phase was generated. Its polarity and amplitude provide important information about the impedance contrast, interface dip, and anisotropic features around the interface. One of the most advantageous features of RF analysis is that the results are not affected by local seismicity. As data from local earthquakes are not required for the analysis, we can construct the subsurface model even at aseismic regions.

By using depth-migrated radial-component RFs with sufficient ray coverage, the RF amplitude can be projected in three-dimensional space and the spatial distribution of seismic velocity interfaces beneath the study region can be constructed (e.g., Shiomi et al. 2008; Ueno et al. 2008). Many studies, including those of Zhu and Kanamori (2000), Shiomi and Park (2008), and Bianchi et al. (2010), have proposed the RF stacking method to estimate the depth of a seismic velocity interface, its plunge azimuth, and/or anisotropic parameters beneath a station. Each stacking method is applied to RFs estimated at a single station. Although their results are estimated independently at each station, the spatial distributions of estimated parameters can be discussed as a comparison with the results for any other stations in the study region.

*Correspondence: shiomi@bosai.go.jp
National Research Institute for Earth Science and Disaster Resilience, 3-1 Tennodai, Tsukuba-shi, Ibaraki 305-0006, Japan

In these RF analyses, neighboring stations generally have similar RFs, especially at sufficient depth compared to station distance.

In the Kii Peninsula, central Japan, non-volcanic low-frequency tremors (LFTs) are actively distributed along the iso-depth contour of the subducting Philippine Sea slab (Obara 2002), as shown in Fig. 1. Because the LFTs are distributed along the down-dip limit of the recurrent megathrust source regions, revealing the structural features near the LFT zone is very important. Shiomi and Park (2008) applied the RF stacking method to the stations in the Kii Peninsula and discussed the spatial distribution of the depth and plunge azimuth of the oceanic Moho discontinuity beneath the seismograph stations. Their results showed large differences between these parameters beneath the two stations at the eastern Kii Peninsula, despite the stations being less than 3 km apart. As Shiomi and Park (2008) used teleseismic events with epicentral distances between 30° and 90°, the incidence angles of teleseismic waves at the bottom of the crust ranged from 25° to 40°. Considering that the Moho depth beneath these stations is 35 km (e.g., Shiomi et al. 2008), the *Ps* conversion points on the Moho discontinuity should overlap greatly over the same region. Thus, it is difficult to explain why the depth and plunge azimuth of the Moho estimated by the RF stacking method have large differences at these proximal stations. On the other hand, there are two other adjacent station pairs in the Kii Peninsula. Although the plunge azimuths beneath the western Kii show large difference, those in the southern Kii and the Moho depth in both regions are almost the same (Shiomi and Park 2008).

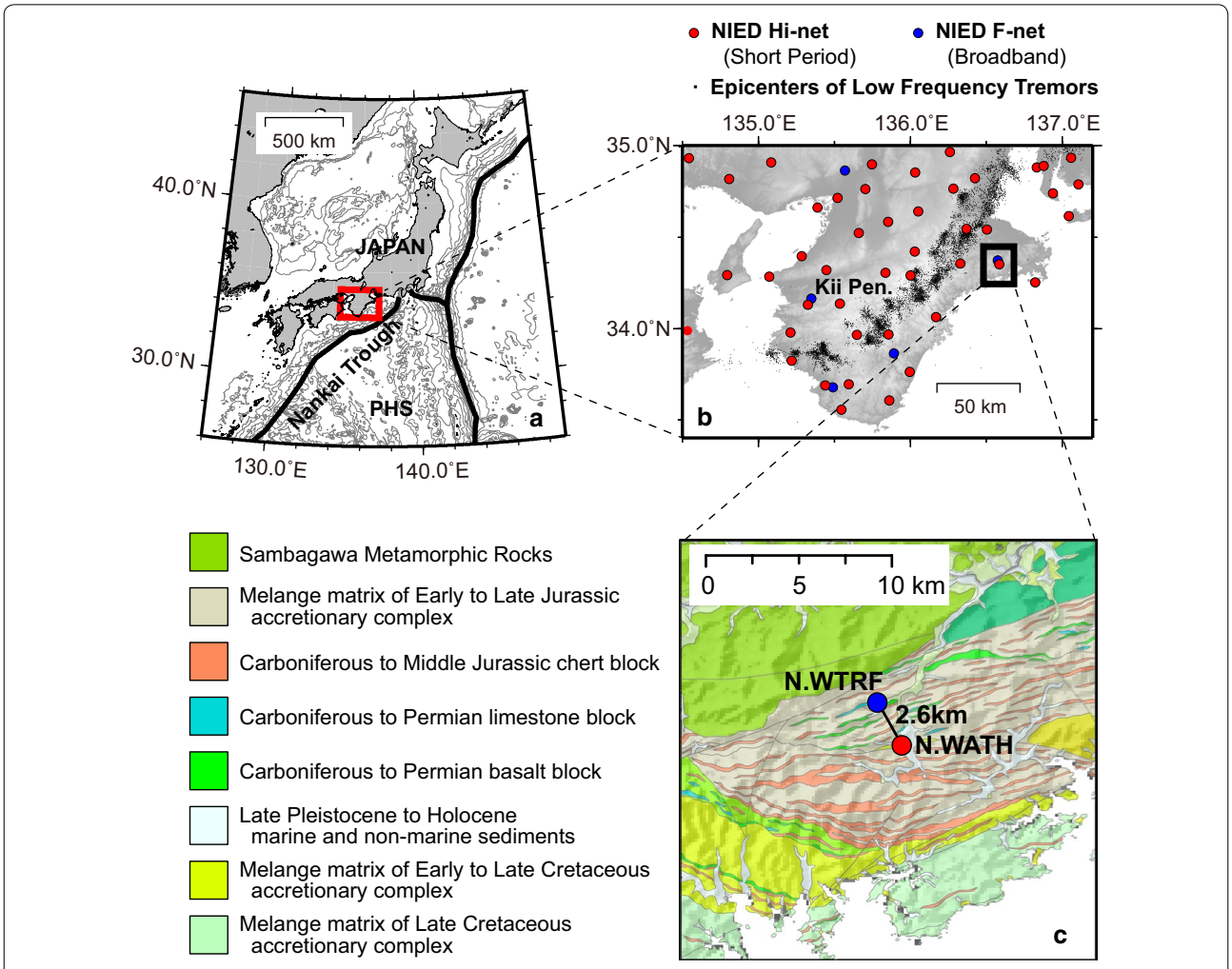

Fig. 1 Location of target stations. **a** Map of the Japan Islands. "PHS" means Philippine Sea plate, which is subducting beneath the southwestern part of Japan from the Nankai Trough. **b** Map of the Kii Peninsula. *Red* and *blue circles* indicate the locations of the NIED Hi-net and F-net stations, respectively. *Black dots* denote epicenters of low-frequency tremors (Maeda and Obara 2009). **c** Detailed locations of N.WTRF (*blue circle*) and N.WATH (*red circle*) on a geological map (Geological Survey Japan, AIST ed. 2015). *Colors* correspond to the surface geology

In this study, we focus first on the similarity and/or dissimilarity of RFs estimated at the pairs of two adjacent stations in the Kii Peninsula. Then, we check the teleseismic waveforms observed at stations in the eastern Kii Peninsula and calculate their cross-correlation coefficients (CCs) to confirm their similarities. Based on qualitative discussion of these data, we propose subsurface models beneath these stations by forward modeling and attempt to explain the reason why dissimilar RFs are estimated at the two adjacent stations in the eastern Kii Peninsula.

Data and methods

At the eastern side of the Kii Peninsula, the National Research Institute for Earth Science and Disaster Resilience (NIED) operates two permanent seismograph stations, named N.WTRF and N.WATH, which are only 2.6 km apart. Figure 1 shows the locations of the two stations on a geological map (Geological Survey of Japan, AIST ed. 2015). Both stations are located in Jurassic accretionary complex with distributions of long and narrow blocks of chert, limestone, and basalt (Fig. 1). N.WTRF is one of the NIED F-net stations, and an STS-2 type broadband seismograph is equipped at the end of the tunnel (Okada et al. 2004). N.WATH is a part of the NIED Hi-net stations. At this station, a three-component short-period velocity seismograph of natural frequency of 1 Hz is installed at the bottom of the borehole at a depth of 110 m. Because the orientations of borehole sensors at NIED Hi-net stations have been estimated by Shiomi (2012), we can compose NS and EW component seismograms from the two orthogonal horizontal waveforms. As we can see in Fig. 1b , there are two other adjacent station pairs in the western and southern Kii Peninsula, respectively. Additional file 1: Figure S1 shows enlarged maps with surface geological information for these additional areas. N.NOKF and N.KMTF are operated as F-net stations, and N.NKMH and N.KTDH are Hi-net stations. Station distances of these pairs are less than 5 km, and surface geological features are much simpler than those in the eastern Kii Peninsula. By comparing these three pairs of stations, we confirm the degree of dissimilarity between the RFs at adjacent stations. Although the type of seismograph used at each station in this study is different, this is not important to the comparison of the RFs because the instrumental response is canceled by the deconvolution process of RF estimation.

Following Shiomi and Park (2008), we selected earthquakes with magnitudes $M \geq 6.0$ and epicentral distances of $30^\circ \leq \Delta \leq 90^\circ$ to estimate the RFs. The motivation of this study was to explain the cause of dissimilar RF observations at two adjacent stations. We chose the teleseismic events between February 2004 and September 2016 and selected waveforms observed simultaneously at both stations with high signal-to-noise ratio to avoid the unknown effects of using different datasets of teleseismic events. We considered a total of 408 events for the N.WTRF–N.WATH pair, 332 events for the N.NOKF–N.NKMH pair, and 353 events for the N.KMTF–N.KTDH pair. As was done by Shiomi and Park (2008), we estimated RFs by the multiple-taper correlation method (Park and Levin 2000). Shiomi and Park (2008) used a low-pass filter with $f_c = 1$ Hz to obtain RFs. In this study, we applied low-pass filters not only with $f_c = 1$ Hz but also with $f_c = 1.5$ Hz to emphasize the dissimilarity between the RFs estimated at two stations by using the higher frequency range.

After a comparison between the estimated RFs and the observed teleseismic waveforms, we constructed simple two-dimensional layered models with anisotropic media to explain the estimated RFs at the N.WTRF and N.WATH stations. Synthetic RFs, whose ray parameters were set to 0.07, were estimated using the computation code developed by Frederiksen and Bostock (2000). When using this code, we set a parameter to calculate the first-order multiples from all layers.

Results and discussion

Estimated receiver functions

Figure 2 shows the RFs at N.WTRF (a, c) and N.WATH (b, d). The positive phases in the radial RFs, shown with blue color in Fig. 2 are converted phases at a velocity interface where the deeper media is faster than the shallower media. In the radial RFs, we can clearly see the arrival of positive *Ps* converted phases at about 4 s (green lines in Fig. 2) at both stations and both frequency ranges. Because this time delay corresponds roughly to the conversion depth of 35 km, these phases were converted at the oceanic Moho discontinuity within the Philippine Sea slab (e.g., Shiomi et al. 2008). For both frequencies, the arrival times of these phases at both stations were almost the same for the backazimuth (BAZ) range of 260°–315°. Checking Fig. 2c, d, which are for the same frequency range as in Shiomi and Park (2008), the Moho-related phases at N.WATH for the BAZ ranges of 0°–60° and 180°–260° arrived slightly earlier and later than those at N.WTRF, respectively. This small difference causes the discrepancy in the estimated Moho parameters obtained using RF stacking analysis. On the other hand, the BAZ dependence of phase arrivals from 0 to 4 s after direct *P*-waves was obviously different between the stations, even for the lower frequency ranges (Fig. 2c, d). Later phases arriving earlier than 4 s were converted at a depth shallower than the Moho. In the radial RFs at N.WTRF, clear positive phases arrived

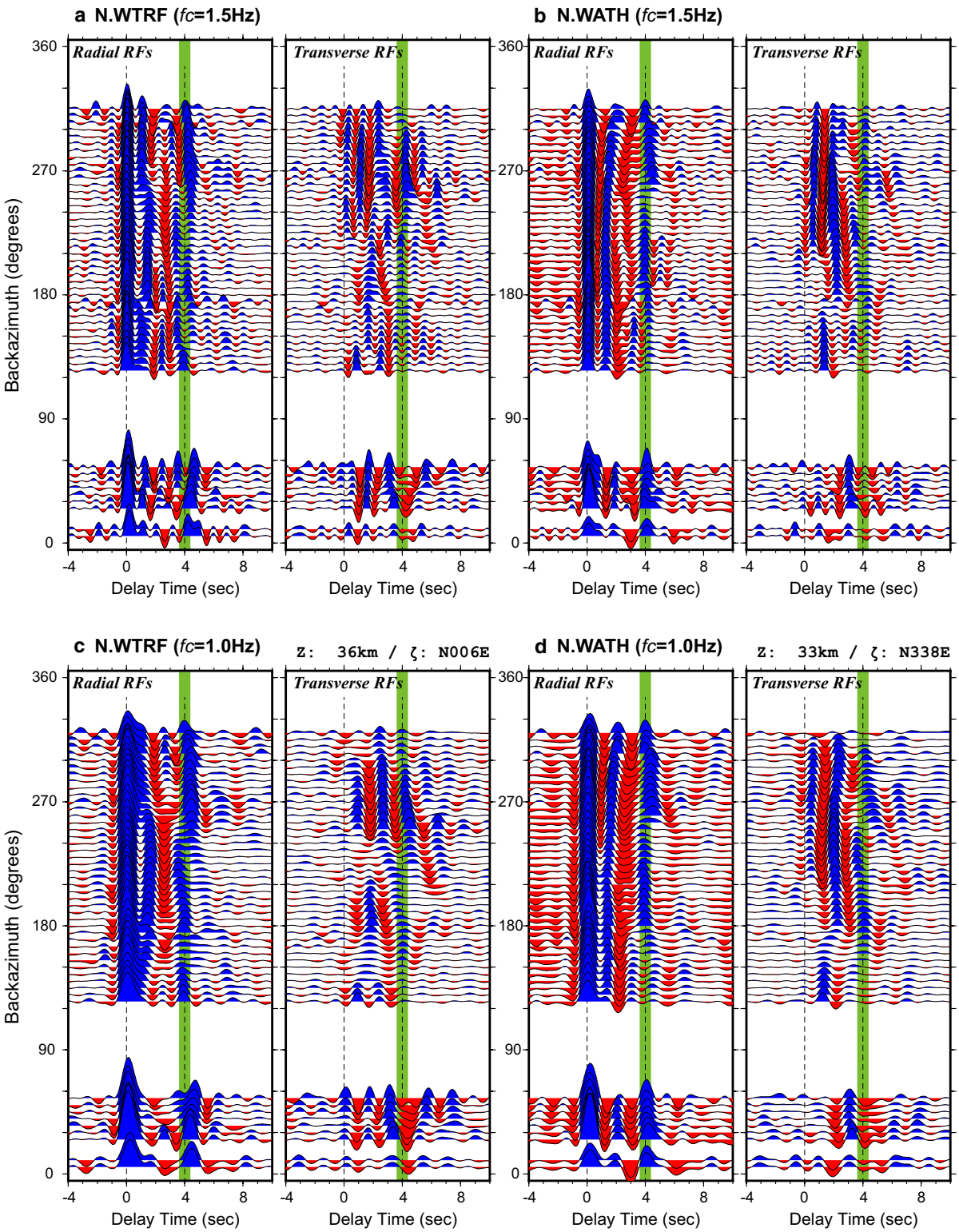

Fig. 2 Estimated receiver functions. Receiver functions observed at N.WTRF (**a**, **c**) and N.WATH (**b**, **d**). Low-pass filters with $f_c = 1.5$ Hz (**a**, **b**) and 1.0 Hz (**c**, **d**) were applied. *Horizontal* and *vertical axes* represent delay time and backazimuth of teleseismic waveforms, respectively. *Vertical green lines* indicate the assumed arrival time of converted phases at the oceanic Moho discontinuity. The depth of Moho discontinuity (z) and plunge azimuth (ζ) reported by Shiomi and Park (2008) are shown on the *right top* of **c** and **d**

around 1 s after the direct *P*-waves for the higher frequency range (Fig. 2a), although the phases were not separated from the direct *P*-waves for the lower frequency range (Fig. 2c). When checking the details, we found that the phases for BAZ ranging from 170° to 260° arrived at about 0.5 s after the phases from other directions. We could not confirm similar features at N.WATH. Although we did also find clear positive phase arrivals around 1 s, the delay times increased gradually for the teleseismic events from west to northwest. The differences between transverse RFs were much clearer. Transverse RFs are affected by the existence of a dipping velocity interface and/or anisotropic material (e.g., Maupin and Park 2009). The similarity of the transverse RFs indicates a similarity of parameters of dipping interfaces and/or anisotropic features beneath the stations. At N.WTRF, large negative (red) and positive phase arrivals were confirmed for the BAZ range of 220°–315° between delay times of 0 and 3 s (Fig. 2a, c). Another positive phase alignment was confirmed from 140° to 220° at 1.5–2.0 s. On the other hand, phases with large amplitudes arrived from the range of 210°–315° at N.WATH between delay times of 0 and 2 s, and these were shifted to the south (180°–270°) in the next time window (2–3 s of delay), as shown in Fig. 2b, d. At the N.WATH station, we observed another positive phase alignment for the BAZ range from 120° to 170° around 1.0–1.5 s in the transverse RFs. The distance between N.WTRF and N.WATH is slightly shorter than the wavelength of *S*-wave with a dominant frequency of 1 Hz and is almost the same as that with a frequency of 1.5 Hz. However, the phase arrival patterns observed at these adjacent stations were clearly dissimilar, even in the case of the lower frequency range. To check whether the dissimilarity of RFs between adjacent stations is usual, we estimated RFs at two other nearby station pairs within the Kii Peninsula (Additional file 1: Figure S1). Additional file 2: Figure S2 and Additional file 3: Figure S3 show the estimated RFs at these stations. From these figures, we could confirm small dissimilarities of RFs with the higher frequency range ($f_c = 1.5$ Hz), especially for the pair in the southern Kii Peninsula (Additional file 3: Figures S3a and S3b). This occurred because the wavelength of *S*-wave with a dominant frequency of 1.5 Hz in the crust is shorter than the distance separating these stations. On the other hand, we could state that similar phase arrival patterns were observed for the longer wavelength range, although the absolute amplitudes were slightly different. Returning to Fig. 2c, d, the latter phase arrival pattern estimated at the stations in the eastern Kii Peninsula is quite different before 4 s, even for the lower frequency range. Considering that the distance between N.WTRF and N.WATH is shorter than those of the two other pairs, we may state that this pair shows quite unusual, but important results and that these features imply that strongly localized anisotropic structures within the crust exist between the two stations. This heterogeneous crust may provide estimates of the Moho parameters.

Cross-correlations of teleseismic waveforms

The distance between N.WTRF and N.WATH corresponds to one wavelength of *S*-wave in the Earth's crust when we consider the seismograms with the $f_c = 1.5$ Hz low-pass filter. Even if the crustal structure beneath the seismograph stations is localized, teleseismic waveforms of wavelength components much longer than the station distance should have high similarity. First, we applied a low-pass filter with $f_c = 0.15$ Hz to the observed teleseismic waveforms and calculated cross-correlation coefficients (CCs) between the same components at these two stations. The results, shown in Fig. 3, confirm that the long-period teleseismic waveforms have high correlation coefficients (>0.7) for all directions and components. This means that the large-scale subsurface structure beneath the two stations is almost the same.

Next, we checked the CCs of teleseismic waveforms after applying a low-pass filter with $f_c = 1.5$ Hz. Figure 4 shows the distribution of the CCs for each component, in the same manner used in Fig. 3. In the case of the higher frequency component, we should consider the time shift for wave propagation between the two stations. In this study, we allowed a time window of ±0.5 s to search for the maximum CCs. In Fig. 4, vertical and radial components show high CCs (>0.6), but the CCs of transverse components are relatively low (~0.4). Transverse teleseismic waveforms from the west showed no correlation (CCs ~ 0.2).

Synthetic RFs

The low CCs found only for the short-period transverse-component teleseismic waveforms support the hypothesis that the existence of strongly localized anisotropic media in the upper and/or middle crust makes *Ps* conversion very complex. As shown in Fig. 1, these stations are located in the Jurassic accretionary complex along the Pacific coast, and Sanbagawa metamorphic rocks are adjacent to the north of N.WTRF. Within the Jurassic accretionary complex at the southern part of N.WATH, long and thin chert blocks are distributed in the east–west direction. In the area between N.WTRF and N.WATH, chert, basalt, and limestone blocks are aligned with ENE–WSW trends. As the geological boundaries in the Kii Peninsula are inclined to the north or northwest and continue to mid-crustal depth (e.g., Ito et al. 2006), this geological feature could be the cause of the difference in the azimuthal anisotropic features beneath these stations.

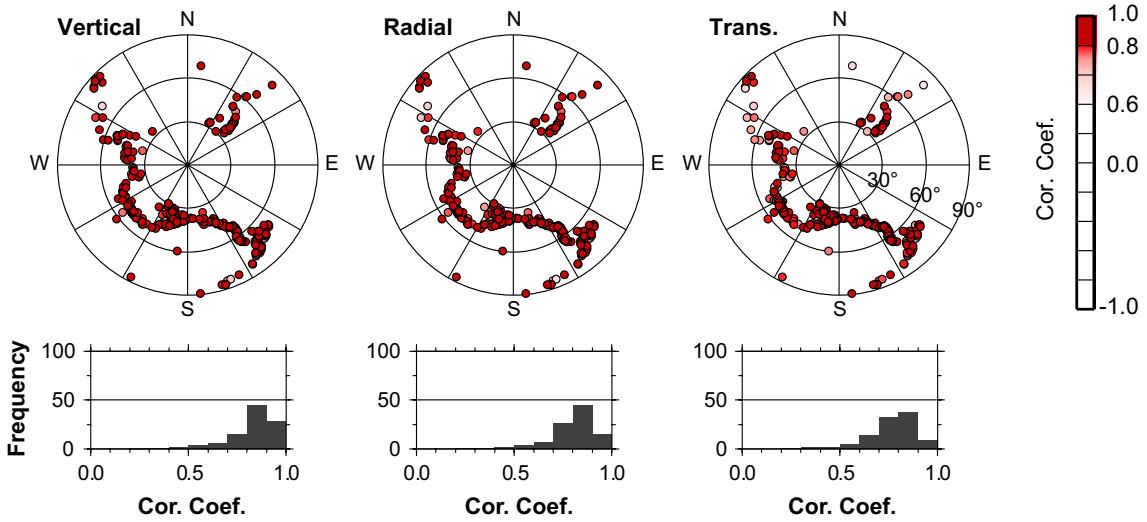

Fig. 3 Distributions of cross-correlation coefficients for long-wavelength teleseismic waveforms. Distributions of cross-correlation coefficients (CCs) between the teleseismic waveforms observed at N.WTRF and N.WATH. A low-pass filter of 0.15 Hz was applied to the seismograms. (*Upper*) Azimuthal distribution of CCs. Radius corresponds to the epicentral distance of each event. *Color* depth corresponds to the CC. (*Lower*) Histograms of CCs. Only the positive coefficient range is displayed because no negative values were detected

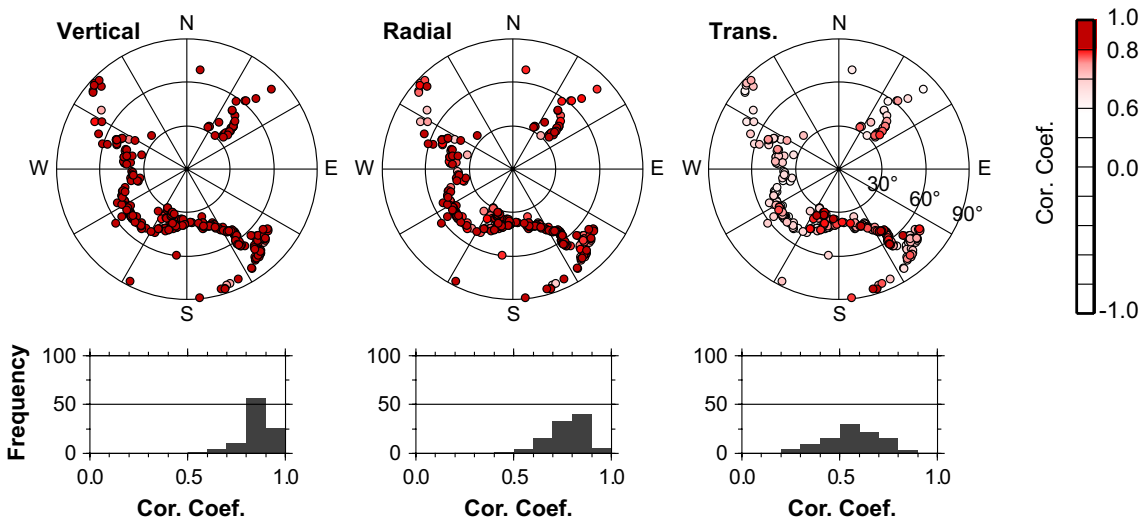

Fig. 4 Distributions of cross-correlation coefficients for short-wavelength teleseismic waveforms. Same as Fig. 4, but a low-pass filter of 1.5 Hz was used

To interpret these features, we constructed simple two-dimensional models by the trial-and-error method. First, we defined the Moho depth as 35 km, based on the result by Shiomi et al. (2008). The *P*-wave velocities (V_P) in the middle crust, lower crust, and uppermost mantle were referred to the results of seismic surveys (e.g., Kodaira et al. 2002; Nakanishi et al. 2002). The ratio of *P*-wave to *S*-wave velocity V_P/V_S was set to 1.732. We set the V_P in the upper crust to 6.3 km/s, but we adjusted the parameters in the upper crust to explain the arrival pattern of the later phases in the estimated RFs.

As a second step, we attempted to estimate the rough thicknesses of the upper, middle, and lower crustal layers to explain the arrival times of positive phases from 1 to 2, 2.5 to 3 s, and at 4 s of N.WATH by the trial-and-error method. Then, we divided each crustal layer into two and added anisotropic parameters to reproduce the azimuthal dependence of the RF amplitude. A steeply north-dipping fast axis in the upper crust was needed to explain the gradual phase delay from 1 to 2 s for the BAZ range of 240°–315°. The result is shown in Table 1 as the N.WATH model.

To construct the N.WTRF model shown in Table 1, we started by modifying the N.WATH model. In the case of N.WTRF, clear positive phases arrived at 1 s, but the phases were delayed by 0.5 s from other directions for the BAZ range of 170°–260°. To reproduce this feature, we did not need a steep symmetry axis, but instead needed a thin anisotropic layer with a fast axis dipping to the NNW direction that was sandwiched by isotropic layers. Thus, we prepared a three-layered upper crust for N.WTRF, although the two-layered model was adopted for N.WATH. We did not have to change the layers deeper than 20 km, corresponding to the lower crust and uppermost mantle, so these two models had the same properties.

Figure 5 shows the synthetic RFs based on these models. As we could reproduce the first clear positive phases that arrived between 1 and 1.5 s, which are converted at the first interface with depth of 3 or 4 km, we insist that reverberations in the shallow crust are not important at these stations even though the stations are located in the accretionary complex.

As shown in Fig. 4, observed transverse components for the earthquakes located in the BAZ which range from 210° to 330° showed very low correlation coefficients. The seismic rays from these directions passed through different geological materials to each station in the eastern Kii Peninsula. The complex geology is the reason why the dissimilar RFs were observed at the two adjacent stations. The trends of the fast axes, 330° for the N.WTRF model and 0° for the N.WATH model, corresponded to the direction perpendicular to the strike of the surface geological boundaries (Fig. 1). Because the surface geological boundaries in the Kii Peninsula are inclined to the north or northwest (e.g., Ito et al. 2006), we propose that the horizontal plane determined by the orthogonal slow and fast axes should be parallel to these boundaries. If this speculation is correct, the slow axis is parallel to the surface geological boundaries. After observing the large transverse RFs in the geologically complex area, the radial RFs needed to be interpreted carefully.

It was still difficult to explain the negative phases that arrived at 3 s in the radial RFs at N.WATH. In general, negative amplitude of RF is caused by the existence of a low-velocity layer. In this study, we set the model to be as simple as possible and did not consider a low-velocity layer. The negative phases between 2 and 2.5 s in Fig. 5b were caused by the apparent low velocity generated by anisotropic crustal media. We already know that there is subducting Philippine Sea slab beneath the stations, and a sedimentary layer, which can be detected as a low-velocity anomaly, may exist above the subducting slab (e.g., Kodaira et al. 2002; Nakanishi et al. 2002). As this layer may be hydrated, we should consider anisotropy within the layer. Moreover, the gray-shaded azimuth in

Table 1 Properties of the synthetic model as defined in Ferra et al. (1991)

Layer index	Layer thickness	V_P	V_S	ρ	Anisotropy				Velocity interface	
					%*P*	%*S*	Fast axis		Strike	Dip
							Trend	Plunge		
N.WTRF model										
U1	4.0	5.80	3.35	2.65	0	0	–	–	–	0
U2	3.0	6.10	3.52	2.75	5	5	330	40	–	0
U3	4.0	6.30	3.64	2.80	0	0	–	–	–	0
M1	4.0	6.60	3.81	2.89	10	10	330	30	–	0
M2	5.0	6.60	3.81	2.89	5	5	240	30	–	0
L1	*7.0*	*6.80*	*3.93*	*2.93*	*0*	*0*	–	–	–	*0*
L2	*8.0*	*6.80*	*3.93*	*2.93*	*10*	*10*	*60*	*0*	*240*	*15*
UM	–	*7.80*	*4.50*	*3.50*	*5*	*5*	*0*	*15*	*240*	*15*
N.WATH model										
U1	3.0	5.80	3.35	2.65	0	0	–	–	–	0
U2	9.0	6.30	3.64	2.80	10	10	0	60	–	0
M1	3.0	6.60	3.81	2.89	0	0	–	–	–	0
M2	5.0	6.60	3.81	2.89	10	10	300	45	–	0
L1	*7.0*	*6.80*	*3.93*	*2.93*	*0*	*0*	–	–	–	*0*
L2	*8.0*	*6.80*	*3.93*	*2.93*	*10*	*10*	*60*	*0*	*240*	*15*
UM	–	*7.80*	*4.50*	*3.50*	*5*	*5*	*0*	*15*	*240*	*15*

Bottom three layers indicated by italics font are the same for both models. Thickness is in km, V_P and V_S are in km/s, and ρ (density) is in g/cm^3

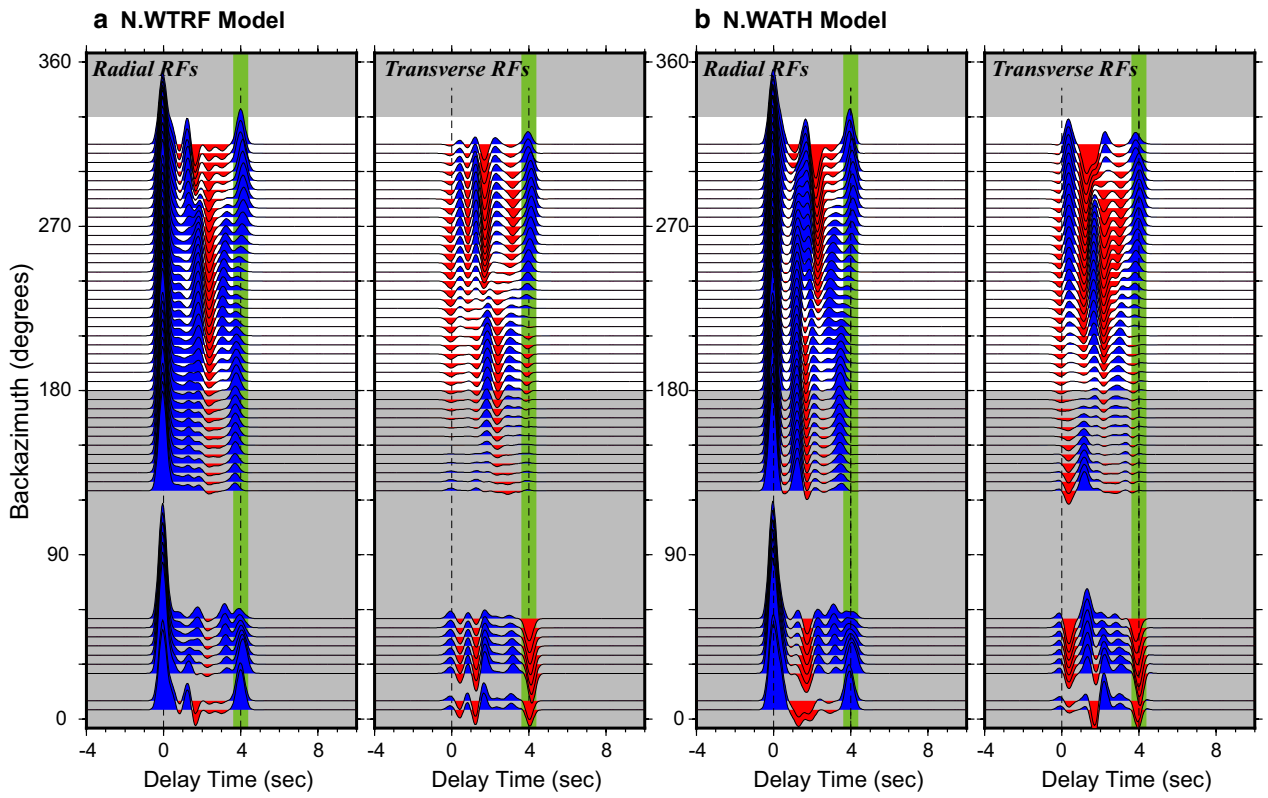

Fig. 5 Synthetic receiver functions based on the model shown in Table 1. Synthetic receiver functions calculated by using the N.WTRF model (**a**) and the N.WATH model (**b**) shown in Table 1. Representation is the same as Fig. 2

Fig. 5 is difficult to explain using our simple models. To reconstruct the complex RFs shown in Fig. 2, a three-dimensional model with curved velocity interface should be considered.

In this study, we obtained a similar later phase arrival pattern for events with BAZ range of 120°–315° by using the subsurface model shown in Table 1. Future work will explain all RFs in detail using a single three-dimensional model.

Conclusions

Receiver function (RF) analysis is often used to reveal subsurface information beneath seismograph stations. When this analysis method is applied to several stations located in close proximity to each other, the observed receiver functions are generally assumed to be similar. In this study, we first introduced different RFs observed at two stations that are proximal to each other and located in the accretionary complex along the Pacific coast of the eastern Kii Peninsula. Large differences, particularly in the time lag before the arrival of the *P*-to-*S* converted phase at the Moho discontinuity, were observed. On the other hand, we also confirmed similar phase arrival patterns in the estimated RFs with lower frequency range ($f_c = 1.0$ Hz) at two other adjacent station pairs in the western and southern Kii Peninsula, respectively. This means that the dissimilarities observed at the eastern Kii Peninsula are unusual, considering that the station distance there is closer than for the two other pairs. A check of the teleseismic waveforms observed at the stations in the eastern Kii Peninsula revealed that the vertical and radial seismograms were quite similar but that the transverse component with low-pass filter of $f_c = 1.5$ Hz had low cross-correlation coefficients. As the wavelength of *S*-wave with a dominant frequency of 1.5 Hz corresponds to the distance of these stations, strongly localized anisotropic crust must exist beneath each station. To verify this assumption, we conducted a synthetic test using two-dimensional simple models with four- or five-layered upper and middle crust. The synthetic RFs were largely different when an anisotropic crust with a steeply dipping symmetry axis and its plunge azimuth was the perpendicular to the strike direction of geological boundaries. This result implies that particular attention must be given to discussing the subsurface structure at geologically complex sites based on RFs, even if the target depth is deeper than the anisotropic materials.

Additional files

Additional file 1: Figure S1. Location of two other station pairs. Map of the two additional station pairs. The stations are less than 5 km apart. Enlarged maps of the western (**a**) and southern (**b**) Kii Peninsula. **c** Map of the Kii Peninsula. Representation is the same as the right-top panel of Figure 1 in the main text.

Additional file 2: Figure S2. Estimated receiver functions at the western Kii Peninsula. Receiver functions observed at N.NOKF (a, c) and N.NKMH (b, d). Representation is the same as Figure 2 in the main text.

Additional file 3: Figure S3. Estimated receiver functions at the southern Kii Peninsula. Receiver functions observed at N.KMTF (a, c) and N.KTDH (b, d). Representation is the same as Figure 2 in the main text.

Acknowledgements
We thank A. W. Frederiksen for providing his synthetic seismogram calculation code and J. Park for sharing his receiver function estimation code. We also thank the anonymous reviewers who carefully reviewed our manuscript and gave us important suggestions for its improvement. We used the Generic Mapping Tools (GMT) (Wessel and Smith 1998) to make the figures in this paper. This study was partially supported by JSPS KAKENHI Grant Number JP16H06475.

Competing interests
The author declares that he has no competing interests.

Received: 27 December 2016 Accepted: 21 March 2017
Published online: 04 April 2017

References

Ammon CJ (1991) The isolation of receiver effects from teleseismic P waveforms. Bull Seismol Soc Am 81:2504–2510
Bianchi I, Park J, Piana Agostinetti N, Levin V (2010) Mapping seismic anisotropy using harmonic decomposition of receiver functions: an application to Northern Apennines, Italy. J Geophys Res 115:B12317. doi:10.1029/2009JB007061
Ferra V, Vinnik LP, Romanowicz B, Kosarev GL, Kind R (1991) Inversion of teleseismic S particle motion for azimuthal anisotropy in the upper mantle: a feasibility study. Geophys J Int 106:421–431
Frederiksen AW, Bostock MG (2000) Modeling teleseismic waves in dipping anisotropic structures. Geophys J Int 141:401–412
Geological Survey of Japan, AIST (ed) (2015) Seamless digital geological map of Japan 1:200,000. May 29, 2015 version. Geological Survey of Japan, National Institute of Advanced Industrial Science and Technology, https://gbank.gsj.jp/seamless/index_en.html. Accessed 8 Feb 2017
Ito K, Umeda Y, Sato H, Hirose I, Hirata N, Kawanaka T, Ikawa T (2006) Deep seismic surveys in the Kinki district: Shingu-Maizuru line. Bull Earthq Res Inst Univ Tokyo 81:239–245
Kodaira S, Kurashimo E, Park J-O, Takahashi N, Nakanishi A, Miura S, Iwasaki T, Hirata N, Ito K, Kaneda Y (2002) Structural factors controlling the rupture process of a megathrust earthquake at the Nankai trough seismogenic zone. Geophys J Int 149:815–835
Maeda T, Obara K (2009) Hypocenter distribution of deep low-frequency tremors in Nankai subduction zone. Jpn J Geophys Res 114:B00A09. doi:10.1029/2008JB006043
Maupin V, Park J (2009) Theory and observations—wave propagation in anisotropic media. In: Romanowicz B, Dziewonski A (eds) Seismology and structure of the Earth, treatise on geophysics, vol 1. Elsevier, Amsterdam, pp 289–321
Nakanishi A, Takahashi N, Park J-O, Miura S, Kodaira S, Kaneda Y, Hirata N, Iwasaki T, Nakamura M (2002) Crustal structure across the coseismic rupture zone of the 1944 Tonankai earthquake, the central Nankai Trough seismogenic zone. J Geophys Res. doi:10.1029/2001JB000424
Obara K (2002) Nonvolcanic deep tremor associated with subduction in southwest Japan. Science 296:1679–1681. doi:10.1126/science.1070378
Okada Y, Ksahara K, Hori S, Obara K, Sekiguchi S, Fujiwara H, Yamamoto A (2004) Recent progress of seismic observation networks in Japan—Hi-net, F-net, K-NET and KiK-net—. Earth Planets Space 56:5–7. doi:10.1186/BF03353076
Park J, Levin V (2000) Receiver functions from multiple-taper spectral correlation estimates. Bull Seismol Soc Am 90:1507–1520
Shiomi K (2012) New measurements of sensor orientation at NIED Hi-net stations. Rep NIED 80:1–20 **(in Japanese with English abstract)**
Shiomi K, Park J (2008) Structural features of the subducting slab beneath the Kii Peninsula, central Japan: seismic evidence of slab segmentation, dehydration, and anisotropy. J Geophys Res 113:B10318. doi:10.1029/2007JB005535
Shiomi K, Matsubara M, Ito Y, Obara K (2008) Simple relationship between seismic activity along Philippine Sea slab and geometry of oceanic Moho beneath southwest Japan. Geophys J Int 173:1018–1029. doi:10.1111/j.1365-246X.2008.03786.x
Ueno T, Shibutani T, Ito K (2008) Configuration of the continental Moho and Philippine Sea slab in southwest Japan derived from receiver function analysis: relation to subcrustal earthquakes. Bull Seismol Soc Am 98:2416–2427. doi:10.1785/0120080016
Wessel P, Smith WHF (1998) New, improved version of the generic mapping tools released. EOS Trans AGU 79:579
Zhu L, Kanamori H (2000) Moho depth variation in southern California from teleseismic receiver functions. J Geophys Res 105:2969–2980. doi:10.1029/1999JB900322